Mon. Not. R. Astron. Soc. **000**, 1–11 (2009) Printed 27 January 2013 (MN LaTeX style file v2.2)

arXiv:1106.1294v1 [astro-ph.CO] 7 Jun 2011

Searching for the trigger of the AGN QPO: 8 years of RE J1034+396

Matthew Middleton[1], Phil Uttley[2] & Chris Done[1]
[1] *Department of Physics, University of Durham, South Road, Durham DH1 3LE, UK*
[2] *School of Physics and Astronomy, University of Southampton, Highfield, Southampton, SO17 1BJ, UK*

27 January 2013

ABSTRACT

RE J1034+396 is one of the most extreme Narrow-line Seyfert 1s detected thus far, showing the only quasi-periodic oscillation (QPO) reliably detected in an Active Galactic Nucleus (AGN). Comparison with similar spectral and timing properties observed in the black hole X-ray binary (BHB) GRS 1915+105 suggests that RE J1034+396 is a super-Eddington accretor. A more complete understanding of the behaviour of RE J1034+396 can therefore lead to a unification of the accretion physics between such extreme AGN and super-Eddington BHBs. Here we report on our latest *XMM-Newton* observations of RE J1034+396, which no longer show the QPO, indicating that this source shows a non-stationary power-spectrum. We use spectral and temporal analysis across all five *XMM-Newton* observations of the source to probe the evolution of the object. The combination of the shape of the fractional variability with energy and the inferred velocity of absorbing material in the line-of-sight rules out an absorption-only method of creating the QPO. Instead the periodically changing absorption may be produced by the QPO causing a change in ionization state.

We extend our analysis by including the covariance spectra which give much better signal to noise than an rms spectrum. These reveal a new aspect of the QPO, which is that there is also a small contribution from a soft component which is hotter than the soft excess seen in the mean spectrum. Folding the lightcurve on the QPO period shows that this component lags behind the hard X-rays. If this is due to re-processing then the lag corresponding to a light travel time across $\sim$30R$_g$. Some of the remaining observations have similar energy spectra and covariance spectra, but none of them show a significant QPO, so we conclude that none of these features are the trigger for the appearance of the QPO in this object.

Key words: accretion, accretion discs – X-rays: binaries, black hole

1 INTRODUCTION

Black holes should be entirely described by their mass and spin, but their observational appearance is also determined by their mass accretion rate. Current models of the accretion flow, both thin disc and hot flow solutions, show that the underlying physics should be fairly scale invariant i.e. the properties of the flow should simply scale mostly with mass for a given mass accretion rate in Eddington units, L/L_{Edd}. Thus data from the well studied, stellar mass black hole binary (BHB) sources can be simply scaled up to describe the supermassive black holes in the center of AGN. There is considerable evidence to support this conjecture. The different spectral states seen as a function of mass accretion rate in BHB may well be seen in AGN (Pounds, Done & Osbourne 1995; Vasudevan & Fabian 2007; Middleton, Done & Gierliński 2007), and 'fundamental-plane' type relations between radio and X-ray luminosity hold across the mass-scale (Merloni, Heinz & di Matteo 2003; Falcke, Körding & Markoff 2004; Köerding et al. 2007). The X-ray timing properties also support a simple scaling argument, with both BHBs and AGN having a similar shape in their broad-band power density spectrum (PDS), but shifted in frequency due to the expected mass-scaling of the characteristic variability time-scales (M^{c}Hardy et al. 2004; Done & Gierliński 2005; M^{c}Hardy et al. 2006).

However, BHBs also often show prominent low frequency quasi-periodic oscillations (LFQPOs) in their X-ray lightcurves (e.g. Remillard & McClintock 2006). These have frequencies from 0.1-10 Hz, so for typical AGN masses these are not detectable given the lightcurves currently available (Vaughan & Uttley 2005). Thus the single signifi-

© 2009 RAS

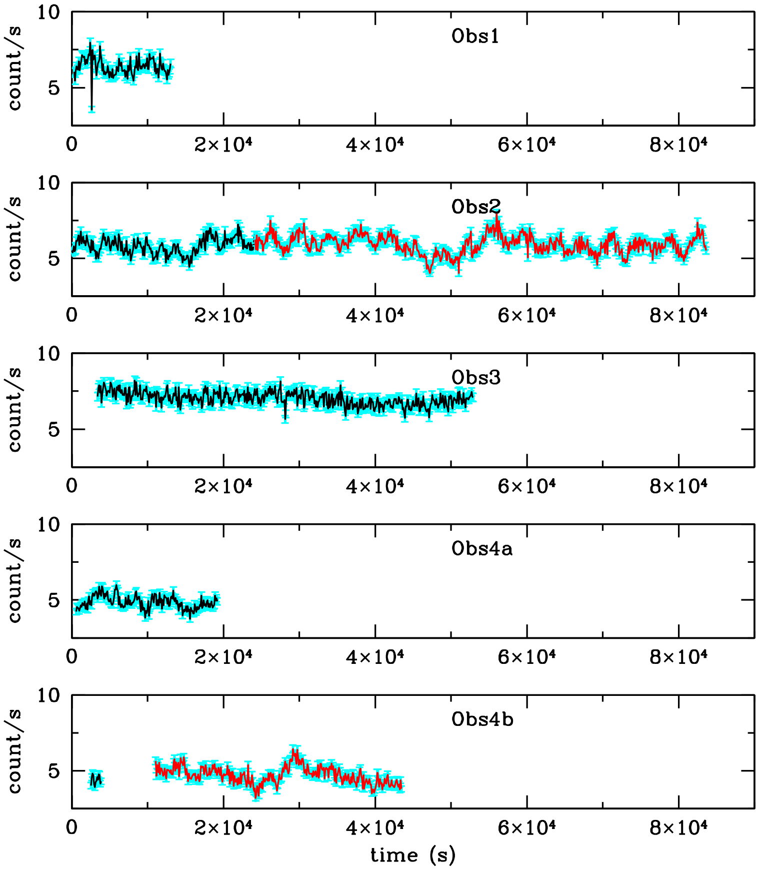

Figure 1. Background subtracted, co-added lightcurves of all five observations of RE J1034+396 taken with *XMM-Newton*, binned on 100 s. Obs1: the first observation (OBSID: 0109070101) of only 16 ks total duration and containing a large amount of background flaring; Obs2: the important second observation containing the QPO (OBSID: 0506440101 showing the 'in-phase' segment of ∼60 ks in red and the remaining lightcurve in black); Obs3: the DDT observation (OBSID: 0561580201) containing ∼50 ks of good data ; Obs4a and 4b the follow-up observation taken in AO9 and broken into two segments the first of which was heavily dominated by background flaring (leaving only ∼ 20 ks of good time) and the second containing moderate flaring episodes leaving 30ks of continuous time (red).

cant AGN QPO, seen in the Narrow Line Seyfert 1 galaxy RE J1034+396 (Gierliński et al. 2008; confirmed using even more robust techniques by Vaughan 2010) is most likely associated instead with the higher frequency QPOs seen in BHBs. These are associated only with very specific spectral states (very high/intermediate), so are much less frequently observed (e.g. Remillard et al. 2002; Remillard & McClintock 2006). While there is currently no reliable mass estimate for this AGN (though recent work is converging on ∼1-4×10^6M$_\odot$: e.g. Bian & Huang 2010; Jin et al. in press), the best match in terms of mass scaled frequency (and L/L$_{Edd}$) appears to be the 67 Hz QPO seen in the probably super-Eddington BHB GRS 1915+105 (e.g. Middleton & Done 2010; Morgan, Remillard & Greiner 1997; Ueda, Yamaoka, & Remillard 2009; Cui 1999; Belloni et al. 2006).

The much longer timescale of the AGN QPO presents an opportunity to examine this feature on the level of individual cycles. This contrasts with the high frequency BHB QPOs which can currently only be studied in a statistical sense by averaging the behaviour over very many cycles, due to the small number of photons detected per cycle. Thus the AGN QPO may give more stringent tests of the origin of this oscillation than the corresponding BHB data.

Both the spectrum and variability of these data can be well modelled using two components, namely an extremely large soft X-ray excess (SX) which remains relatively constant on the timescale of the QPO, together with a weak power law tail to higher energies which is strongly modulated on the QPO timescale (Middleton et al. 2009). Models of the complete spectral energy distribution (SED) of this object show that the SX is the dominant component of the total bolometric luminosity of ∼5×10^{44}erg s^{-1} (Puchnarewicz et al. 1998; Wang & Netzer 2003; Casebeer et al. 2006; Middleton et al. 2007; Jin et al. in press), giving L/L$_{Edd}$ ∼ 4-1 for the black hole mass range of 1-4× 10^6M$_\odot$ discussed above. Thus the equivalent sources in terms of high Eddington fraction are GRS 1915+105 (see above), which has been accreting at or above Eddington for more than 20 years (e.g. Truss & Done 2006) and probably also the Ultra-luminous X-ray Sources (ULXs; see Fabbiano 1989; Miller & Colbert 2004; Roberts 2007). Both of these can show an SED dominated by a similarly distorted 'hot disc' component to that which forms the SX in RE J1034+105 (Zdziarski et al. 2003; Middleton et al. 2009; Gladstone, Roberts & Done 2009).

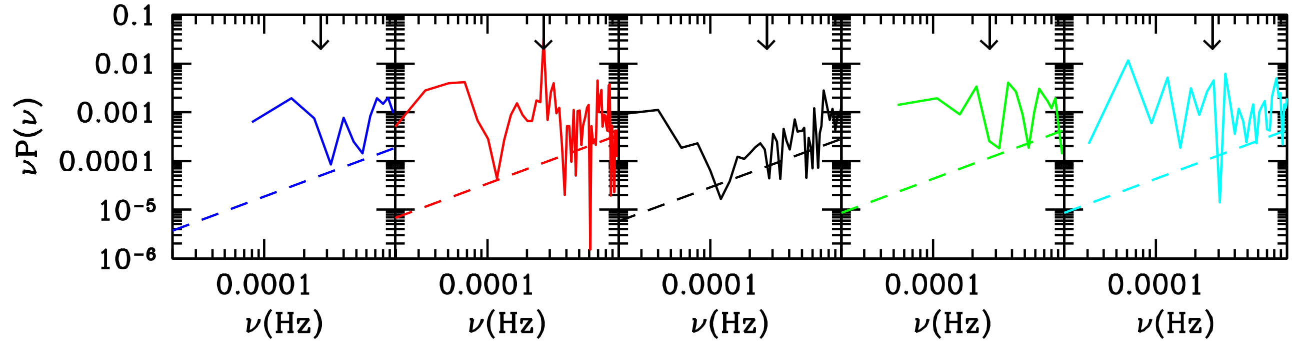

Figure 2. The PDS of Obs1 (blue), Obs2 (red), Obs3 (black) and Obs4 (a: green and b: cyan) made from a single realisation of the variability (thus no error-bars are shown as they are, by definition, the size of the power itself), including statistical white noise, the level of which is indicated by the dashed line. The PDS of the follow-up observations do not show the highly significant QPO seen at $\sim 2.7\times10^{-4}$Hz in Obs2, indicated by the arrows.

Date	OBSID	Full exposure (to nearest ks)	Good exposure (all detectors)	Mode
01-05-2002	0109070101	16	–	FW
31-05-2007	0506440101	93	84	FW
31-05-2009	0561580201	70	50	SW
09-05-2010	0655310101	52	20	SW
11-05-2010	0655310201	54	30	SW

Table 1. Useful information about each of the five *XMM-Newton* observations. FW indicates that the observation was taken in Full-Window mode and SW indicates that Small-Window mode was used.

In this paper we analyse three new observations of RE J1034+396 obtained by *XMM-Newton*, together with the previous two data sets (including the one with the QPO detection). The QPO is plainly not detected in the first and third of the new datasets, but we may be seeing residual signs of its presence in the second. We look at the corresponding spectral evolution of the source, to try to identify what triggers the appearance (and disappearance) of the QPO.

2 DATA EXTRACTION

In this paper we will compare the spectral and timing properties of all five observations of RE J1034+396 with *XMM-Newton*. For each observation we use 45" regions and extract co-added MOS and PN, background subtracted lightcurves (using SAS V9.0/10.0) to maximise signal to noise (see details of extraction method in Gierliński et al. 2008 and Middleton et al. 2009). The dates, OBSIDs, total exposure time, useful exposure time and operational mode are provided in Table 1.

The first two observations (hereafter Obs1 and Obs2) were carried out in full-window mode and so are piled up in all 3 detectors due to the extremely soft nature of the source. Obs1 is also heavily contaminated by soft protons, with strong background flares across almost all the observation. Any conservative background selection would give almost no usable data. Including all the data gives the lightcurve shown in Fig 1a with the one low point marking the position of the largest background flare.

Obs2 is much less affected by background and we use the same good time intervals as Gierliński et al. (2008). Fig 1 shows the ~50 ks segment of the ~90 ks in which the QPO is most coherent and this feature is discussed at length in Gierliński et al. (2008) and Middleton et al. (2009).

Two further observations have been taken of RE J1034+396 since the QPO detection, the first was through director's discretionary time in AO8 (Obs3 hereafter) where the level of flux can be seen to have risen, and the second was taken in AO9 and was broken into 2 ~ 50ks pointings (Obs4a and 4b hereafter). All of these were taken in small window mode and so are not piled up.

2.1 Power spectra

Figure 2 shows the corresponding PDS (plotted as frequency×power, where power is normalised to fractional rms^2) of the lightcurves shown in Figure 1. The 100s binning of the lightcurves gives a Nyquist frequency (and hence upper limit on the frequency on which the PDS can be determined) of 5×10^{-3}Hz. The PDS includes the Poisson white noise component which starts to dominate at high frequencies, with normalisation given by the error bar variance on each point as shown by the dotted line on each figure.

While the PDS of Obs2 shows a significant QPO (>3σ, even when applying the most stringent Bayesian analyses - see Vaughan 2010), the PDS of Obs1, Obs3 and Obs 4a/b do

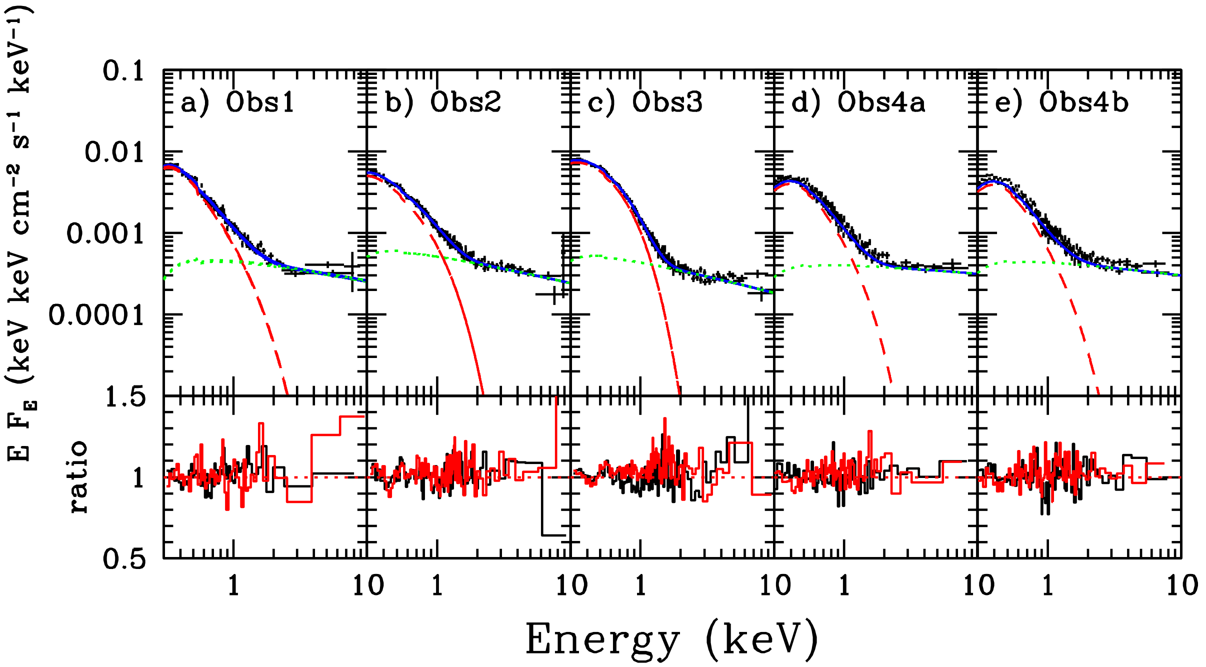

Figure 3. Time-averaged X-ray spectra of all five observations of RE J1034+396 taken with *XMM-Newton*. The data and best-fit unfolded model are absorbed with a minimum column equal to Galactic n_H and are composed of a low-temperature thermal Compton component (red) and high-temperature thermal Compton component (green) which are convolved to give the total model (blue). Residuals to the fit are shown in the panels below and clearly demonstrate the presence of soft atomic features.

Obs	TBABS	COMPTT				NTHCOMP		χ^2 (d.o.f.)
	$n_H \times 10^{20}$cm^{-2}	T_0 (keV)	kT_e (keV)	τ	Flux ($\times 10^{-12}$)	Γ	Flux ($\times 10^{-12}$)	
1	$2.82^{+1.09}_{-0.85}$	$0.038^{+0.015}_{-peg}$	$0.281^{+0.019}_{-0.050}$	$9.0^{+1.4}_{-peg}$	10.09	$2.24^{+0.21}_{-0.24}$	2.33	227 (215)
2	$1.47^{+0.12}_{-peg}$	$0.033^{+0.006}_{-peg}$	$0.195^{+0.018}_{-0.014}$	$14.1^{+1.3}_{-1.0}$	6.84	$2.33^{+0.08}_{-0.09}$	2.62	390 (355)
3	$1.47^{+0.15}_{-peg}$	$0.030^{+0.009}_{-peg}$	$0.140^{+0.004}_{-0.003}$	$21.5^{+0.9}_{-0.9}$	11.22	$2.37^{+0.06}_{-0.07}$	2.19	511 (350)
4a	$1.47^{+0.64}_{-peg}$	$0.072^{+0.005}_{-0.011}$	$0.220^{+0.291}_{-0.063}$	$12.3^{+6.5}_{-8.3}$	6.50	$2.11^{+0.15}_{-0.47}$	2.18	223 (246)
4b	$1.47^{+0.003}_{-peg}$	$0.073^{+0.003}_{-0.004}$	$0.253^{+0.305}_{-0.081}$	$10.1^{+5.3}_{-5.4}$	6.21	$2.17^{+0.15}_{-0.13}$	2.31	340 (297)

Table 2. Best-fit model parameters with 90% confidence limits where given. Note that the values for Obs1 are not well constrained due to the shorter duration of the observation. Importantly however, the higher quality data in the latter two observations gives us confidence in our interpretation. Where the error limit is given as *peg*, this indicates the parameter has pegged at its hard limit. In the case of n_H this is the Galactic value of 1.47×10^{20}cm^{-2} , in the case of τ this is 9 (to produce constrained fits) and in the case of T_0 this is 0.01 keV. The units of flux for each individual component are erg s^{-1} cm^{-2} integrated over the 0.3–10 keV bandpass.

not have a similarly significant feature at this frequency. In particular, Obs3 sets very stringent limits on the presence of a similarly strong QPO, Thus the QPO is not persistent, strengthening its association with the transient high-frequency (HF) QPOs seen in BHBs (Middleton & Done 2010) rather than the much more ubiquitous LFQPOs (Remillard & McClintock 2006).

We use the maximum likelihood fitting routine of Vaughan (2010), assuming an intrinsic power law PDS ($P(f) \propto f^{\alpha}$) plus white noise, where α is -0.90 ± 0.17, -1.48 ± 0.32 and -1.59 ± 0.23 for Obs3, Obs4a and 4b respectively, compared to -1.80 ± 0.20 for Obs2 (consistent at the 2σ level with our more simplistic fit of -1.35 - see Gierliński et al. 2008). These indices are poorly constrained in Obs4a/b due to the relatively short lengths of the continuous lightcurves, but Obs3 is significantly different to Obs2. This change in red noise and QPO properties means that the PDS is non-stationary. This is even more dramatic than in NGC4051 (Miller et al. 2010), which was the first non-stationary AGN PDS.

3 X-RAY SPECTRA

As both Obs1 and 2 are heavily piled up we attempt to mitigate the worst of the effects (i.e. migration of counts from soft to hard energies). In the case of Obs1, centroid removal is prohibitively expensive in terms of counts, so instead we

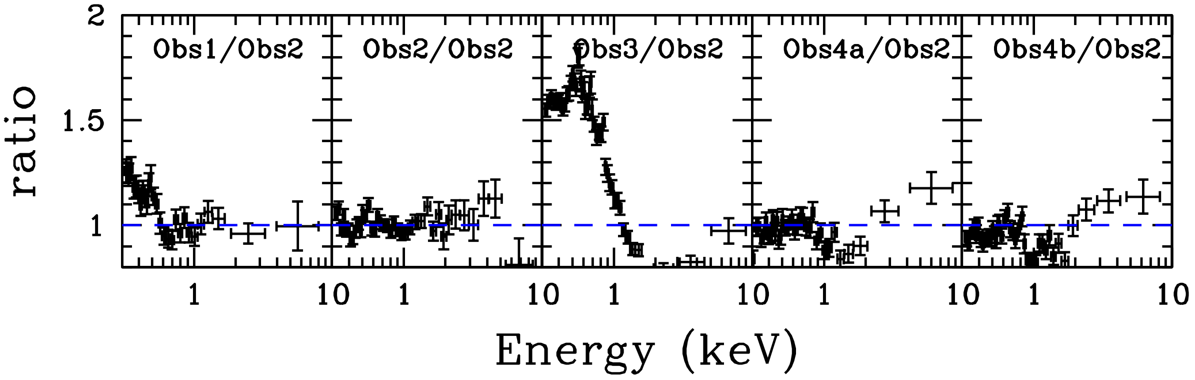

Figure 4. Ratios of the MOS1 data to best-fitting model of Obs2. Whilst the soft component is clearly more dominant in Obs1 and Obs3, in the 2 parts of Obs4 the soft component is consistent with that when the QPO is present.

extract the X-ray spectrum from single patterns only. Obs2 is substantially longer and so we remove an inner centroid of 7.5" to account for the worst effects of pile-up. We extract and fit MOS spectra only, due to the mismatch between MOS and PN spectra at low energies, using XSPEC v11.3.2.

We apply the best-fitting model of Middleton et al. (2009): a low-temperature, optically thick thermal Comptonisation of (unobservable UV/EUV) disc seed photons, together with high-temperature, optically thin Comptonisation which dominates at high energies (in XSPEC this is TBABS*(COMPTT+NTHCOMP)). The low temperature Comptonisation component (COMPTT here) is similar to that invoked for high signal-to-noise ULX (Gladstone et al. 2009) which, if composed of high stellar mass black holes ($\leq 100\mathrm{M}_\odot$) rather than intermediate mass BHs, would share similar Eddington/super-Eddington mass accretion rates as inferred for RE J1034+396. We fit this model to the spectra of all five observations (Fig 3), with model parameters and their 90% confidence limits presented in Table 2.

Fig 4 shows the ratio between the MOS1 data for each non-QPO observation to the best fitting spectral model for Obs2. These ratio plots show that the soft component is relatively stronger in Obs1 and Obs3 than in Obs2, but Obs4a/b have spectral shapes which are very similar to that seen when the QPO was observed though with apparant stronger warm absorber features at ∼ 0.9–2 keV. The SX variability is clearly associated with an intrinsic change rather than decreased absorption as the column density pegs at the lower limit of absorption in our Galaxy ($1.47\times10^{20}\mathrm{cm}^{-2}$, taken from the $\mathrm{n_H}$ tool[1]) except for Obs1 where pileup/background issues mean the spectra are not reliable. Whilst the first three observations appear to have broadly consistent parameters for the shape of the components, their normalisations differ, with Obs2 having a lower SX component (see also Fig 2). Conversely, Obs4a and 4b appear to have an increased seed photon and electron temperature for the SX, with a less steep tail to high energies, though the ratio of flux in SX and tail is similar to Obs2 (see also Fig 2).

3.1 RGS spectra

The flux ratios in Fig 4 and residuals to the spectral fits (lower panels in Fig 3) indicate the presence of soft absorption features which may be consistent with a 'warm absorber' (Kaastra et al. 2000; Kaspi et al. 2000a). We use the RGS to search for atomic features associated with this, but the poor signal-to-noise means that we need to co-add datasets. The previous section has already shown that there are significant spectral changes between observations, and even in a single observation (Obs2) there are subtle changes in the spectrum with time. In particular, the dip in the lightcurve of Obs2 (Fig1b) at ∼ 40-50 ks, possibly due to an occultation event as seen in other AGN (McKernan & Yaqoob 1998; Gallo et al. 2004; Risaliti et al. 2007; Turner et al. 2008), has a clear energy dependence (Figure 1 of Middleton et al. 2009), while Maitra & Miller (2010) see subtle spectral changes in atomic features correlated with the QPO. Nonetheless, due to the limited statistics, we choose to co-add all the data from Obs2 and Obs3 in order to get the most sensitive limits on the time averaged spectral properties.

We analyse the RGS spectrum in detail, fitting individual Gaussian lines to the spectrum, following the algorithm of Page et al. (2003) with equivalent width (EW), σ and centroid wavelength as free parameters. The results of this are shown in Fig. 5 for each arm of the RGS separately (red and black), with wavelength scale corrected for the source redshift. We show the fit parameters along with likely identification in Table 3 for lines seen in both arms at $>3\sigma$ significance ($\Delta\chi^2 > 9$), or for lines at this significance which are seen in only one arm if the other arm has no data at that wavelength range. We ignore any features close to data gaps. The majority of these features have a small outflow velocity, of order 1000s km/s, showing that they are most probably associated with a wind from the broad line region/torus. Material from closer in to the accretion disc would most probably have much higher velocity. The line widths also imply a similar turbulent velocity of $\sim 400 - 1000$ km/s, again arguing strongly against an inner disc origin for this material.

We fit these features with an ionised absorption model, XSTAR (grid25BIG with 200 kms^{-1} turbulent velocity -

---

[1] http://heasarc.gsfc.nasa.gov

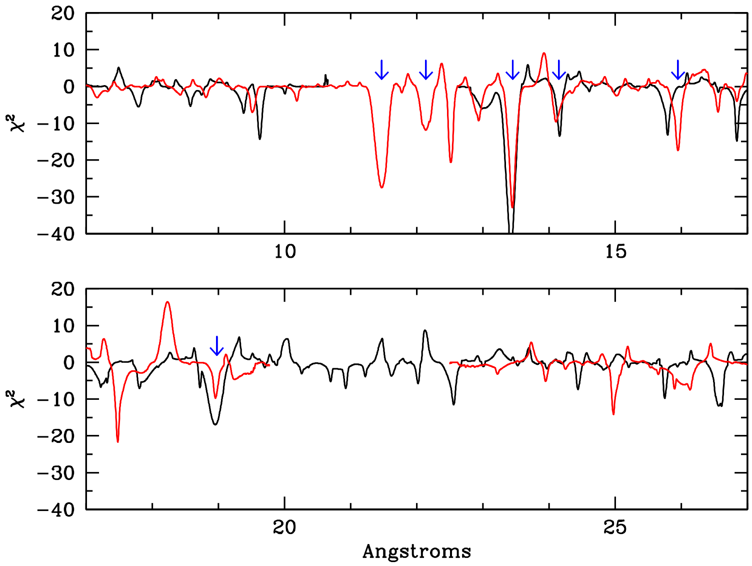

Figure 5. Co-added RGS spectra from Obs2 and Obs3 showing each respective arm (arm 1 in black, arm 2 in red), with the best fitting Gaussian lines from the algorithm of Page et al. (2003), corrected for the source redshift of 0.042. The properties of each line marked with an arrow is given in Table 3.

species	$\lambda_{\rm obs}$(Å)	$\lambda_{\rm lab}$(Å)	z (km s $^{-1}$)	EW (Å)	σ (km s^{-1})
Fe XIX	13.43	13.53	-2200 ± 350	0.071	475
Fe XVIII	14.13	14.21	-1700 ± 300	0.049	300
Fe XVIII	15.87	16.08	-3900 ± 300	0.078	225
OVIII	18.96	18.97	-200 ± 250	0.047	175
Fe XXII*	11.47	11.77	-7600 ± 400	0.096	2000
Fe XXI*	12.14	12.28	-3400 ± 350	0.059	1850

Table 3. Average line parameters from running the Gaussian line fitting algorithm of Page et al. (2003) where both arms of the detector register a significant feature ($\Delta\chi^2 > 9$) or it is significantly detected in one over a gap in the other (denoted by *). The $\lambda_{\rm obs}$ values are corrected for the source redshift of 0.042 and are compared to the rest frame wavelengths of the ionised species to determine the Doppler shift of the absorbing material (given to the nearest 100 km s^{-1}). The errors on the redshift velocities are given to the nearest 50 km s^{-1} and are determined assuming the an error on the observed wavelength of 0.15 m$\AA$, i.e. half the width of the spectral binning.

Reeves et al. 2008), together with an absorbed, low-temperature Compton component to account for the continuum. The inclusion of a column of 2.23×10^{21}cm^{-2} and ionisation, log$\xi = 2.7$ gives an improvement in χ^2 of 116 for 2 d.o.f, where the strongest predicted features are from ionised populations of Oxygen, Neon and Iron. This column and ionisation parameter are similar to those derived by Maitra & Miller (2010) from the lower resolution EPIC spectra of Obs2, but their time resolved analysis suggested that these absorption features changed with the QPO period, so they suggest that the QPO is caused by an orbiting cloud. However, the $\sim$ 3700 s period coupled with the likely mass of 2×10^{6}M$_\odot$ requires that the cloud is at a distance of only 15 R_g. This is completely incompatible with the relatively low velocity of this material seen in both the turbulence and outflow in these higher resolution RGS spectra.

Maitra & Miller (2010) suggest that a change of >30% in ionistion fraction would be required to explain the changes seen based on the phase binned EPIC spectra of Obs2. We perform a similar phase binned selection process with the higher resolution (although lower SNR) RGS data of Obs2 alone and fit this with narrow absorption of the soft continuum and find that the major difference between the two data sets is the change in continuum normalisation (at $\sim$ 6% as expected from the periodic behaviour) with a <3σ difference in $\Delta\chi^2$ when the ionistaion parameters are the same (log$\xi \sim 3$ and overall fit quality of 903/898). This suggests that, rather than an absorbing column creating the QPO, the correlated absorption features are instead due to material in the line of sight responding to a changing illumination. This sets only a limit on its density, that $n > 7 \times 10^7$ cm^{-3}, in order that the material can recombine on timescales substantially less than the period (e.g. McHardy et al 1995).

4 ENERGY-DEPENDENT VARIABILITY

The PDS and mean X-ray spectra allow us to quantify the variability and spectral behaviour when averaged over energy and time respectively. However, it is possible to use

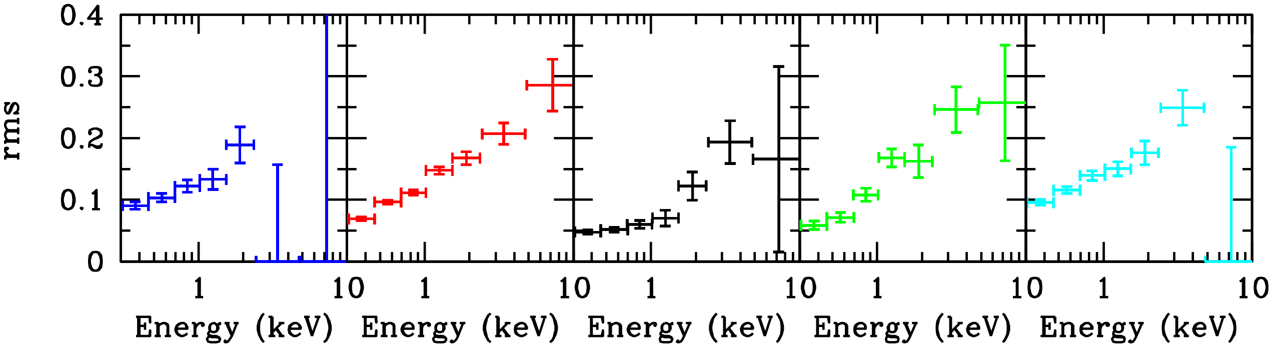

Figure 6. rms spectra of all four observations made using co-added, background subtracted lightcurves. Whilst pile-up will have an effect on the observations taken in full window mode (Obs1 - blue and Obs2 - red) this should only provide a small constant offset as the variability transfer is from soft energies where the stable spectral component dominates.

more sophisticated spectral-timing tools which explore the amplitude of variability as a function of energy.

4.1 RMS spectra

The fractional root-mean-square variability amplitude (rms hereafter: Edelson et al. 2002; Markowitz, Edelson & Vaughan 2003; Vaughan et al. 2003) gives a simple view of the energy-dependence of the variability. In essence, it involves taking a lightcurve in each energy band and then plotting the fractional rms of each light curve as a function of energy. This was done for the Obs2 data in Middleton et al. (2009), where the strong rise in rms as a function of energy almost exactly mirrored the ratio of hard power-law to soft excess component derived from the X-ray spectrum. This lends support to the two-component spectral decomposition, with the two components having different variability properties. Most of the short term variability is associated with the power-law component, but this is increasingly diluted at low energies by the increasing contribution of the mostly constant soft component.

We show the fractional rms spectra of all 5 observations in Fig 6 using 100s binning for the co-addded (MOS and PN), background subtracted lightcurves in each energy band. We use the total Obs2 lightcurve, not just the segment where the QPO is 'in-phase', and do not exclude the central section of the image to mitigate pileup in either Obs1 or Obs2 as this leads to an unacceptable loss of counts.

All the rms spectra show a broadly similar shape, with rms increasing as a function of energy, but with subtle differences in terms of the gradient at high and low energies. To quantify this we fit a straight line function to the log-linear data and determine the reduced χ^2 in each case. These are 0.62, 1.04, 2.47, 1.43 and 0.90 for the 5 observations respectively and demonstrate that the greatest deviation from the shape of the fractional variability in Obs2 is Obs3 due to the increase in the SX component.

We convert the fractional rms spectra into absolute rms spectra in counts units by multiplying by the mean count rate (from the summed lightcurves over all 3 detectors) in each band, and then using the instrument response to fit this in XSPEC. This shows the variable spectral shape directly (e.g. Revnivtsev et al. 2006; Sobolewska & Zycki 2006). Fig 7 shows this for Obs3, where the dashed line shows a SX scaled so that the integrated flux is equal to that of the time-averaged component relative to the power-law flux. Plainly, the SX seen in the rms variability is much smaller (by a factor 16) than this, but is consistent with the same shape. The flux in the variable hard component is 1.2×10^{-12} erg s^{-1} cm^{-2}, compared to 2.5×10^{-12} erg s^{-1} cm^{-2} in the variable part of the soft component. Thus while some of SX variability could be driven by reprocessing of the illuminat-

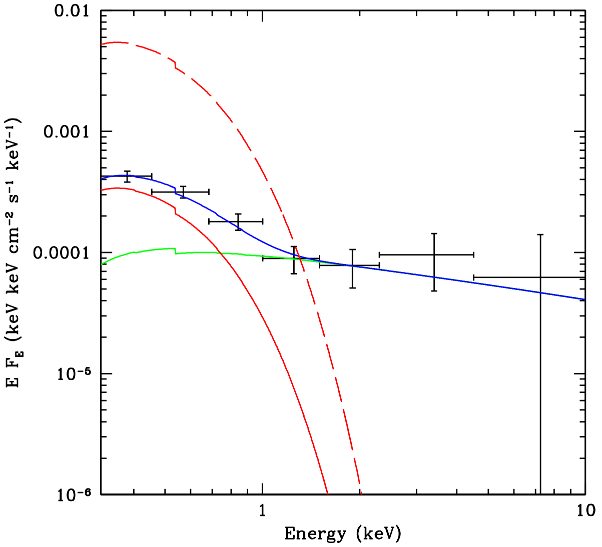

Figure 7. Spectrum of the absolute rms of Obs3 made by multiplying the rms by the mean counts in each band (summed over the 3 detectors) and folding with a suitably binned spectral response. We apply the best fitting spectral model of cool thermal Comptonisation (red) together with hot thermal Comptonisation (green) which convolve to give the total spectrum (blue) which is absorbed by a neutral column. The best-fit differs from the time-averaged spectrum in having a greater relative contribution from the hard component as can be seen by the predicted level of the soft component assuming the same contribution as the X-ray spectrum (red dashed line). The size of the error-bars demonstrates that this method of analysing the variability properties of each spectral component is very poorly constraining due to the low signal-to-noise.

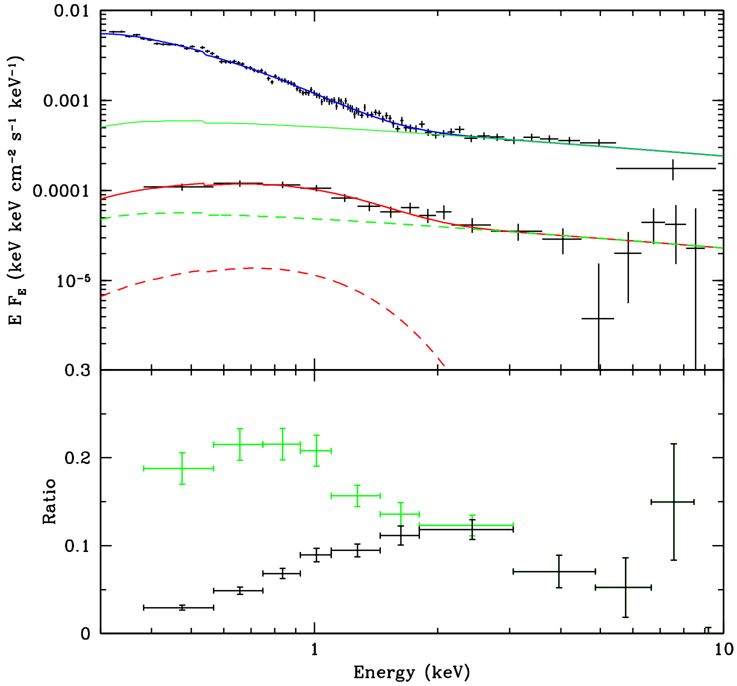

Figure 8. *Upper panel*: time-averaged Obs2 spectrum showing the MOS1 data together with the best-fitting model in blue and the power-law component in solid green. The covariance spectrum at the QPO frequency is shown with its best fitting model in red and power-law component in dashed green. *Lower panel*: The shape of the coherent rms at the QPO frequency can be re-extracted by obtaining the ratio of the covariance to the time-averaged spectrum (black). As seen in Middleton et al. (2009) the shape increases up to ∼ 3 keV but after this is poorly constrained. By obtaining the ratio of the covariance data to the power-law component of its best-fitting model (green) we can see the shape of the variable SX. This peaks at a significantly higher temperature than the stable time-averaged SX which suggests that this is a different component.

ing hard tail, this is unlikely to be the explanation for all of it.

4.2 Covariance spectra

We can improve upon the poor statistical quality of the rms spectrum by measuring the covariance (Wilkinson & Uttley 2009). This method works by cross-correlating each narrow energy band with a much broader reference band, which effectively acts as a matched filter to pick out correlations, so greatly reducing the noise. By dividing the measured covariance by the absolute rms of the reference band, we can obtain a covariance spectrum in detector counts, similar to the absolute rms spectrum but with much smaller error bars. Provided that the underlying variations between bands are spectrally coherent (i.e. well-correlated), this technique is so effective at improving the statistics of the rms spectrum that the variability can be sampled over multiple frequency band-passes by selecting bin sizes and length of segments over which the rms is averaged). We extract the covariance spectra (relative to the 0.36-2.16 keV band) from the PN data as this provides us with the highest quality data from an individual detector. Guided by the results in Middleton et al. (2009), we split Obs2 into three frequency bands, covering long timescales (0.01-0.2 mHz), the QPO (0.2-0.4 mHz) and short timescales (0.4-2 mHz). By comparing these covariance spectra, it becomes possible to determine which spectral component is dominating the variability over a given frequency range, e.g. at the frequency of the QPO.

Fig 8a shows the spectrum in the QPO band (red) compared to the time averaged spectrum (blue). The shape is similar to that of the rms spectrum from Obs3 shown in Fig 7 in that it is steeper than the power law tail in the mean spectrum. A single power law fit has index is $\Gamma = 3.2 \pm 0.3$ compared to 2.3 in the mean spectrum, and also requires significant absorption of $N_H = 0.10 \pm 0.05$ cm^{-2} in order to fit the turn-down at the lowest energies. While this is a good fit, with $\chi^2_\nu = 40/50$, the energy dependence of the QPO supports instead a two component model. Although folding aperiodic noise on a given period can produce misleading results (Benlloch et al. 2001) the red noise is dominated by the periodic process on the QPO frequency in Obs2. Fig 9a shows the resulting folded lightcurve of the QPO as a function of energy, i.e. the lightcurve in a given energy band folded on the QPO frequency. These suggest that there is a small lag from hard to soft energies which is quantified in Fig 9b which shows that the lightcurve above ∼1 keV leads the soft bands by ∼0.1±0.01 cycles, hence we fit the two component model which fits the mean spectrum. We first let only the normalisations of these two components be free but this results in an unacceptable fit with $\chi^2_\nu = 72/51$, with residuals concentrated at low energies. We additionally allow the shape of the soft excess to be free and find a much better fit ($\chi^2_\nu = 38/48$) for significantly higher electron and seed photon temperatures of $kT_e = 0.31 \pm 0.10$ keV and

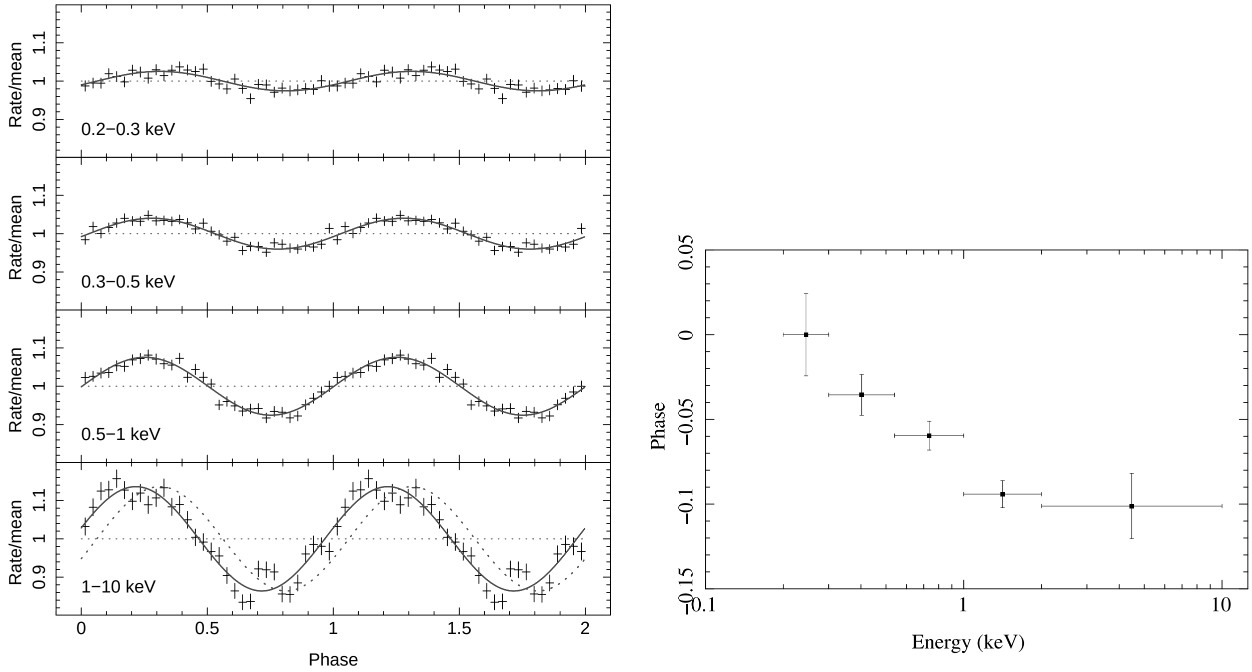

Figure 9. *Left*: shows the lightcurve folded on the QPO period in different energy bands. The dotted line suggests that the hard (1-10 keV) emission leads the soft (0.2-0.3 keV) emission by ∼ 370 s. *Right*: the phase-energy plot of the folded lightcurves showing the constrained phase shift of 0.1±0.01 cycles above 1 keV.

$kT_0 = 0.12 \pm 0.05$ keV,respectively. Alternatively, a single blackbody component with $kT = 0.17 \pm 0.03$ keV also fits the shape of the soft component in the QPO ($\chi^2_\nu = 39/49$).

Thus one attractive possibility is that the soft lag is due to reprocessing, with the QPO in the hard tail also giving a QPO in the illuminating spectrum seen by the accretion disc. The energetics are again an issue as the reflection albedo of the disc should be quite high, however, with the soft component flux of 2.6×10^{-13} ergs cm^{-2} s^{-1}, comparable to 4.3×10^{-13} ergs cm^{-2} s^{-1} of the hard component it appears plausible that the soft component is made via reprocessing.

Fig 10 shows the covariance spectra at the QPO timescale (0.2-0.4 mHz: black) compared to that of the longer (0.01-0.2 mHz: red) and shorter (0.4-2 mHz: green) timescale variability. The rapid variability is somewhat harder than the QPO but still contains a similar but smaller hot, soft component. This subtle difference between the QPO and rapid variability is not at all evident from the rms spectra alone (Middleton et al 2009). It is only revealed by these better signal-to-noise covariance spectra. However, the change in spectral shape between the QPO and long timescale variability is so large that this is clear even in the rms spectra (Middleton et al 2009).

The remaining observations have insufficient variability power at the QPO frequency to make covariance spectra in the narrow QPO energy band, so we use only two frequency bands, covering long (0.02-0.2 mHz) and short (0.2-2 mHz) timescale variability, and compare these to the same frequency bands in Obs2, where 'short' corresponds to the co-added QPO and rapid variability spectrum. The short timescale covariance spectra are shown in Fig 11a. Obs4a and b are very similar to Obs2, showing the hotter soft excess component which is present in the QPO however Obs3 (black) is slightly softer, appearing to peak at lower temperatures consistent with the SX in the mean spectrum. Fig 11b shows the corresponding plot for the long timescale variability, showing clearly that this is dominated by the soft excess in all observations with a shape similar to the SX component in the time-averaged spectrum.

5 DISCUSSION

Understanding the variability of RE J1034+396 is important as the significant QPO (in Obs2) makes it unique amongst AGN. The QPO is plainly not present in Obs3, showing that the QPO is transient rather than a long-lived feature of the lightcurve. Comparing the spectral and timing properties of the average and frequency binned data allows us to compare and contrast the physics whilst the QPO was present and not present. This also allows us to test some of the proposed models for the QPO (e.g. Maitra & Miller 2010; Das & Czerny 2010).

All of the observations are consistent with a two component continuum, with a strong soft excess and weak high energy tail. The strength and shape of the soft excess clearly varies between observations, while the (much lower signal to noise) power law tail remains fairly constant. However, on much shorter timescales (within a single observation) this behaviour is reversed. The fractional r.m.s as a function of energy shows that the soft excess is always much less variable than the tail, especially on the most rapid timescales. The dominance of the soft excess in the energy spectrum means that this strongly dilutes the amount of rapid variability at low energies as in Middleton et al (2009).

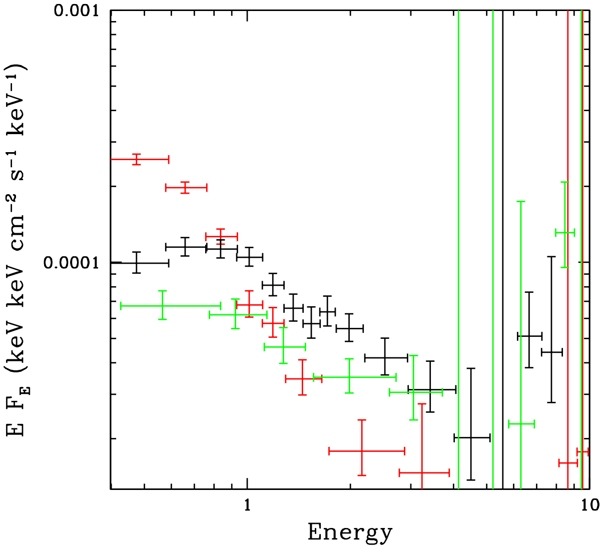

Figure 10. The covariance spectra from Obs2 on short (green: 0.4-2 mHz), QPO (black: 0.2-0.4 mHz) and long (red: 0.01-0.2 mHz) timescales. The short timescale variability is similar to that of the QPO, but has less of the hot soft component in its spectrum. The long timescale variability is similar in shape to the soft excess seen in the mean spectrum.

However, we now go beyond this and look in detail at the spectrum of the variability using the much better signal-to-noise covariance spectra. This reveals a new aspect of the QPO itself (0.2-0.4 mHz variability i.e. 5000-2500s timescale), which is that, as well as the power law tail, it also has additional variability at lower energies. This component is clearly hotter than the soft excess seen in the mean spectrum, and the reality of this as an additional component is supported by it lagging behind the 2-10 keV variability by 370 s. This lag could be produced by reprocessing, in which case it corresponds to a light crossing distance of $30R_g$ for a $2 \times 10^6 M_\odot$ black hole.

This new information on the QPO spectral shape puts some constraints on models. For example, a radial perturbation of the Compton torus leads to an offset geometry i.e. to elliptical orbits whose perihelion precesses. However, there is no change in illumination of the disc during the azimuthal precession so it is hard to incorporate a soft lag from reprocessing into this model. Conversely, a vertical oscillation or coupled vertical-radial oscillation clearly changes the disc illumination (Abramowicz & Kluzniak 2005; Blaes et al 2007).

An alternative set of models incorporate a transonic shock rather than a global mode. The shock could occur in a hot, very low angular momentum flow, and its radial position can oscillate (Das & Czerny 2010). The maximum in hard X-ray flux is where this shock radius is largest, which leads also to stronger illumination of the disc, so these models can also produce a soft lag from reprocessing.

The QPO spectrum is also clearly not affected by strong absorption features. An absorption origin for the QPO is also ruled out by the RGS spectrum which shows that the atomic features (which are present in the spectrum as claimed in Maitra & Miller 2010) are narrow and not strongly Doppler shifted. The small distances required for periodic obscuration by an orbiting clump of material to produce the QPO would imply much larger velocities. The periodic change in absorption seen by Maitra & Miller (2010) may instead simply be the wind at large distances changing in ionisation in response to the changing illuminating flux.

None of the remaining observations show any significant excess of power over the red noise at the QPO frequency. The one with the most power at this frequency is Obs4b, which, along with Obs4a, has a fairly similar short timescale covariance spectrum to that of the QPO which may indicate a similar variablity process was occuring although not as dominant as in Obs2.

Thus the QPO is transient, and there is no clear trigger for its emergence. One potential way forward is instead to assume that this is similar to the 67Hz QPO in GRS 1915+105 (e.g. Morgan, Remillard & Greiner 1997) and use the substantially larger dataset on GRS 1915+105 to search for the trigger of the QPO in the stellar mass black hole. This has not yet been done, but may prove to be illuminating.

6 CONCLUSION

RE J1034+396 is one of the most extreme and important AGN detected thus far as its timing properties resemble those of the highest luminosity BHBs. Follow-up observations show that the PDS no longer contains the strong QPO that characterised the lightcurve in the 2008 detection. Such a change in the intrinsic variability properties indicates that the PDS is non-stationary.

We use covariance spectra to get better signal to noise on the spectrum of the variability. This reveals new features in the QPO itself. There is a soft component in addition to the power law tail which contributes to the QPO signal. Folding the lightcurve on the QPO timescale over different energy bands indicates that this component lags behind the hard emission. This implies a size scale of $\sim 30R_g$ if this is produced by reprocessing of the hard QPO spectrum, though we caution that the lag could also be caused by a more complex interaction between the disc and corona, rather than by reprocessing. However, a reprocessing origin puts some constraints on the QPO mechanism, since this requires a changing illumination of the disc. This probably rules out models where the QPO is from a radial perturbation precessing around the black hole, as here there is no change in disc illumination. Instead this could be produced by a vertical or coupled vertical-radial (breathing mode) mode (Abramowicz & Kluzniak 2005; Blaes et al 2007), or the oscillating shock model of Das & Czerny (2010).

We rule out occultation models from an orbiting cloud from the RGS data, which show that the ionised absorbed has narrow features at low velocity, unlike those expected from material within $20R_g$ as required by the QPO timescale.

None of the other 4 datasets show the QPO despite 3 of these showing rather similar spectra and 2 of these showing a rather similar covariance spectrum on short timescales. Thus there is no clear trigger we can identify for the QPO from these data. We suggest instead that it may be useful to search the much more extensive datasets in black hole binaries for the trigger of their transient high frequency QPOs.

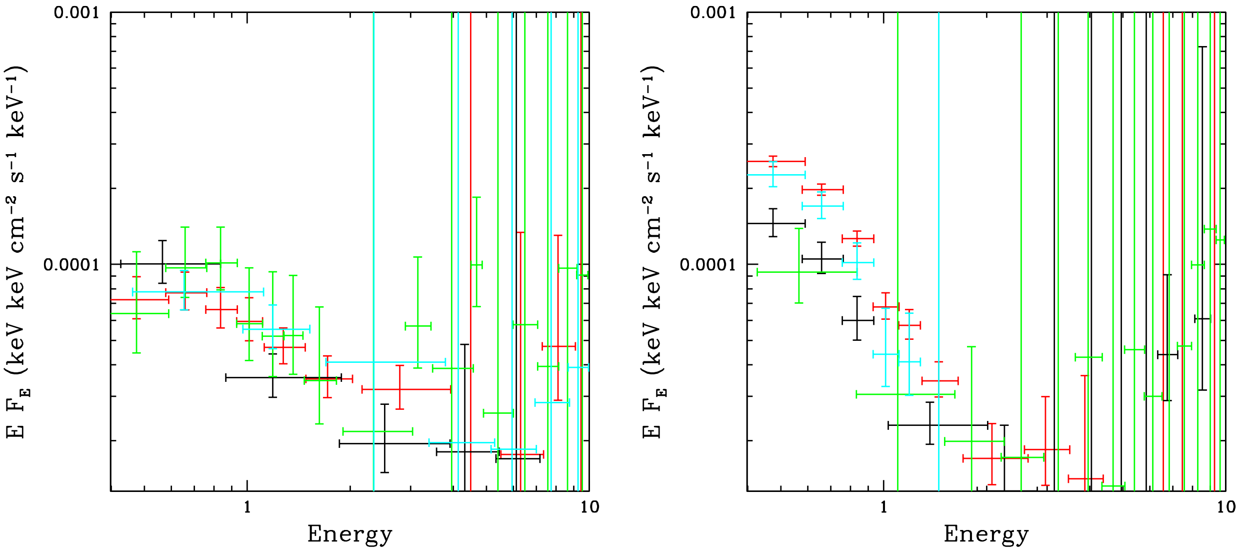

Figure 11. *Left*: The covariance spectra of the short timescale variability of the 4 well constrained observations of RE J1034+396 (red: Obs2, black: Obs3, green: Obs4a, cyan: Obs4b). The shape of the SX variability looks like that of the time-averaged SX in Obs3 but that of Obs4 (a and to a lesser extent b) looks similar to that of the QPO variability where a dissimilar component is present. *Right*: The analogous plot of the long timescale variability where all shapes look similar to the time-averaged SX component.

7 ACKNOWLEDGEMENTS

We thank the anonymous referee for their useful insights and suggestions. MM and CD acknowledge support from STFC via a standard grant and PU via an STFC advanced fellowship. This work is based on observations obtained with *XMM-Newton*, an ESA science mission with instruments and contributions directly funded by ESA Member States and NASA. We thank Dr Mat Page for his assistance with the line-finding algorithm that he generously provided and Dr Simon Vaughan for his excellent Bayesian R routines.

REFERENCES

Abramowicz M. A., Kluźniak W., 2005, Ap&SS, 300, 127
Belloni T., Soleri P., Casella P., Méndez M., Migliari S., 2006, MNRAS, 369, 305
Bian W.-H., Huang K., 2010, MNRAS, 401, 507
Blaes O. M., Šrámková E., Abramowicz M. A., Kluźniak W., Torkelsson U., 2007, ApJ, 665, 642
Casebeer D. A., Leighly K. M., Baron E., 2006, ApJ, 637, 157
Cui W., 1999, ASPC, 161, 97
Das T. K., Czerny B., 2010, arXiv, arXiv:1009.3615
Done C., Gierliński M., 2005, MNRAS, 364, 208
Edelson R., Turner T. J., Pounds K., Vaughan S., Markowitz A., Marshall H., Dobbie P., Warwick R., 2002, ApJ, 568, 610
Fabbiano G., 1989, ARA&A, 27, 87
Falcke H., Körding E., Markoff S., 2004, A&A, 414, 895
Gallo L. C., Boller T., Tanaka Y., Fabian A. C., Brandt W. N., Welsh W. F., Anabuki N., Haba Y., 2004, MNRAS, 347, 269
Gierliński M., Middleton M., Ward M., Done C., 2008, Natur, 455, 369
Gladstone J. C., Roberts T. P., Done C., 2009, MNRAS, 397, 1836
Kaastra J. S., Mewe R., Liedahl D. A., Komossa S., Brinkman A. C., 2000, A&A, 354,
Kaspi S., Brandt W. N., Netzer H., Sambruna R., Chartas G., Garmire G. P., Nousek J. A., 2000, ApJ, 535, L17
Körding E. G., Migliari S., Fender R., Belloni T., Knigge C., McHardy I., 2007, MNRAS, 380, 30
Maitra D., Miller J. M., 2010, ApJ, 718, 551
Markowitz A., Edelson R., Vaughan S., 2003, ApJ, 598, 935
McHardy I. M., Papadakis I. E., Uttley P., Page M. J., Mason K. O., 2004, MNRAS, 348, 783
M^{c}Hardy I. M., Koerding E., Knigge C., Uttley P., Fender R. P., 2006, Natur, 444, 730
McKernan B., Yaqoob T., 1998, ApJ, 501, L29
Merloni A., Heinz S., di Matteo T., 2003, MNRAS, 345, 1057
Middleton M., Done C., 2010, MNRAS, 403, 9
Middleton M., Done C., Gierliński M., 2007, MNRAS, 381, 1426
Middleton M., Done C., Ward M., Gierliński M., Schurch N., 2009, MNRAS, 394, 250
Miller M. C., Colbert E. J. M., 2004, IJMPD, 13, 1
Miller L., Turner T. J., Reeves J. N., Lobban A., Kraemer S. B., Crenshaw D. M., 2010, MNRAS, 403, 196
Page M. J., Soria R., Wu K., Mason K. O., Cordova F. A., Priedhorsky W. C., 2003, MNRAS, 345, 639
Pounds K. A., Done C., Osborne J. P., 1995, MNRAS, 277, L5
Puchnarewicz E. M., Mason K. O., Siemiginowska A., 1998, MNRAS, 293, L52
Reeves J., Done C., Pounds K., Terashima Y., Hayashida K., Anabuki N., Uchino M., Turner M., 2008, MNRAS, 385, L108
Remillard R. A., McClintock J. E., 2006, ARA&A, 44, 49
Remillard R. A., Muno M. P., McClintock J. E., Orosz J. A., 2002, ApJ, 580, 1030
Revnivtsev M., et al., 2006, A&A, 447, 545
Risaliti G., Elvis M., Fabbiano G., Baldi A., Zezas A., Salvati M., 2007, ApJ, 659, L111
Roberts T. P., 2007, Ap&SS, 311, 203
Sobolewska M. A., Życki P. T., 2006, MNRAS, 370, 405
Truss M., Done C., 2006, MNRAS, 368, L25
Turner T. J., Reeves J. N., Kraemer S. B., Miller L., 2008, A&A, 483, 161
Ueda Y., Yamaoka K., Remillard R., 2009, ApJ, 695, 888
Vasudevan R. V., Fabian A. C., 2007, MNRAS, 381, 1235

Vaughan S., 2010, MNRAS, 402, 307
Vaughan S., Edelson R., Warwick R. S., Uttley P., 2003, MNRAS, 345, 1271
Vaughan S., Uttley P., 2005, MNRAS, 362, 235
Wang J.-M., Netzer H., 2003, A&A, 398, 927
Wilkinson T., Uttley P., 2009, MNRAS, 397, 666
Zdziarski A. A., Lubiński P., Gilfanov M., Revnivtsev M., 2003, MNRAS, 342, 355